IEEE Access
Multidisciplinary | Rapid Review | Open Access Journal

Received September 10, 2020, accepted September 19, 2020, date of publication September 30, 2020,
date of current version October 12, 2020.

Digital Object Identifier 10.1109/ACCESS.2020.3027798

Using Lumped Element Equivalent Network Model to Derive Analytical Equations for Interpretation of Transformer Frequency Responses

BOZHI CHENG[1], (Graduate Student Member, IEEE), ZHONGDONG WANG[1,2], (Senior Member, IEEE), AND PETER CROSSLEY[1], (Senior Member, IEEE)

[1]Department of Electrical and Electronic Engineering, The University of Manchester, Manchester M1 7JP, U.K.
[2]College of Engineering, Mathematics and Physical Sciences, University of Exeter, Exeter EX4 4QF, U.K.

Corresponding author: Zhongdong Wang (zhongdong.wang@exeter.ac.uk)

This work was supported in part by National Grid, Warwick, U.K.

ABSTRACT Frequency Response Analysis (FRA) is regarded as the most effective technique for detecting mechanical faults in transformer windings. However, the main challenge in applying the FRA technique lies in the correct interpretation of the differences between the diagnosis and the reference frequency spectra. A transformer can be modeled as an equivalent circuit network comprising inductances (L) and capacitances (C), where L and C are electrical parameters dependent on the winding geometry; a relationship exists between the winding geometry, the electrical components of the equivalent circuit network and the measured FRA spectra. Through electromagnetic circuit analysis, this paper provides a theoretical basis to develop a fundamental understanding of FRA spectra and their resulting interpretation. The FRA spectra are first explained for a single air core winding with uniform structure, and then the complexity is gradually increased by taking into consideration the iron core, the mutual inductive coupling between parts of the same winding and then between the separate windings of the transformer. Mathematical expressions are developed to represent the relationship between the FRA characteristics and the corresponding electrical components of the equivalent circuit network model.

INDEX TERMS Transformer modeling, Frequency Response Analysis (FRA), interpretation, electrical circuit analysis.

NOMENCLATURE

μ_r	Real part of permeability of electrical steel in per unit value
μ_i	Imaginary part of permeability of electrical steel in per unit value
C_s	Winding series capacitance
C_g	Winding shunt capacitance to ground
α	Space coefficient
L_{core}	Magnetizing inductance of winding
$\boldsymbol{L}_{air}$	Air core inductance of winding
$\boldsymbol{\beta}$	Magnetic coupling factor between parts of winding with iron core present
$\boldsymbol{\beta}_{air}$	Magnetic coupling factor between parts of air core winding
$\boldsymbol{C}_{es}$	Equivalent series capacitance of winding seen from tested winding terminals in a transformer
$\boldsymbol{C}_{eg}$	Equivalent winding shunt capacitance to ground seen from tested winding terminals in a transformer
n	Number of stages/sections in a lumped element equivalent circuit network model
ω	Angular frequency
N	Voltage ratio of high voltage to low voltage windings of transformer

The associate editor coordinating the review of this manuscript and approving it for publication was Mehdi Bagheri.

I. INTRODUCTION

Frequency Response Analysis (FRA) is the most sensitive technique available for detecting mechanical winding faults in a power transformer. The underlying principle is physical displacement or deformation of a winding results in changes in the equivalent electrical components of the winding, and

as the frequency response is measured over a frequency range from a few Hz to several MHz, these variations in the inductances (L) and capacitances (C) modify the locations and/or numbers of resonances in the FRA amplitude spectrum.

As transmission voltages increase over the years, transformers need to face more stringent requirements of Basic Insulation Levels (BIL). Therefore winding structures evolve, either from a single helical to a double helical or multi-layer winding; or from a plain disc to an intershielded or interleaved disc winding. Different winding designs, applied by transformer manufacturers, intrinsically increase the variations of characteristics in the measured FRA spectra.

The challenge of FRA technique lies in the correct interpretation of the measured FRA spectra. Statistical indices were used to objectively assess the differences in the FRA spectra measured before and after the fault [1], [2], as produced by either laboratory experiments [3], [4] or simulation studies [5]–[8]. Artificial intelligence (AI) was also used to process the FRA data to identify winding faults [9], [10]. Nevertheless, a quantitative relationship linking winding geometry, equivalent electrical components, and the corresponding FRA measurement results is still desirable. In this respect, mathematical expressions were developed in [11] to correlate natural frequencies of a ten-element equivalent circuit network model with each individual electrical component of the winding, and the correlations were verified using artificially created winding models and simulation results. The delta- and star-connection of the three-phase windings were then considered, nevertheless, other important influencing factors such as magnetizing inductance and the interaction between primary and secondary windings were not included in this mathematic derivation exercise. When winding design data was not accessible, attempts to establish transformer models and to correlate the measured frequency responses with the corresponding electrical components, or even the geometric information, of windings, were carried out using various optimization algorithms such as Genetic Algorithm [12], Gauss-Newton Iteration Algorithm [13] and Particle Swarm Optimization Algorithm [14]. Unfortunately, there is no IEC/IEEE standard for FRA interpretation at current stage, although a CIGRE Working Group A2.53 has recently been established and is now preparing a FRA technical brochure.

Electromagnetic circuit theory is applied in this paper to model a transformer, and mathematical expressions are developed based on a circuit representation of the transformer to describe the relationship between FRA characteristics and the equivalent electrical components. Equation derivation first considers single air core windings, and then the influencing factors are considered sequentially; the complexity is increased by the inclusion of the iron core, and then the mutual inductive coupling between parts of a winding, and inductive and capacitive coupling between two windings within the same phase.

It should be mentioned that the FRA spectra in this paper are produced by the end-to-end open circuit FRA measurement method [15]–[17]. All the windings modeled and analyzed in this paper are of uniform structure, i.e. the same conductor, and equal number of turns per disc and non-grated insulation along the entire winding. This is not an unusual assumption when considering the standardized design and manufacture practice introduced in 1980s. Nevertheless, practical cases such as tap winding inclusion are not considered here. In addition, the winding terminal conditions, such as the bushing and measurement set-up, are ignored for simplicity, and the derived equations do not consider losses as they do not shift the resonant frequencies but only produce a damping effect [6].

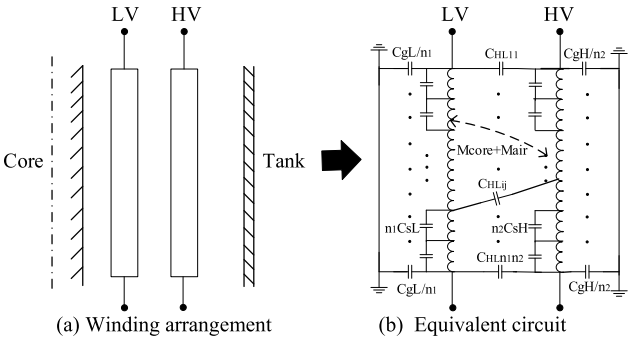

FIGURE 1. Circuit model for single phase two-winding transformer.

II. SINGLE PHASE TWO WINDINGS TRANSFORMER

A 144/13 kV 60 MVA single phase two-winding transformer model was constructed based on real transformer design data; the low voltage (LV) winding is a single helical winding of 13 kV with 74 turns of conductor and the HV winding is an interleaved disc winding of 144 kV with 140 discs. **FIGURE 1**(a) shows the half axis-symmetric cross-sectional diagram and **FIGURE 1** (b) the equivalent circuit model, where each lumped unit represents either a double discs of the disc type winding or a turn of the single helical/multi-layer winding, of which the electrical parameters are calculated based on winding geometry. By applying basic Circuit Analysis Theory onto the network model, the end-to-end open circuit frequency responses can be calculated. The methodology to establish the equivalent circuit network model has been verified in [6], [7].

TABLE 1 lists the electrical parameters and their total values, which are calculated based on winding geometry; the magnetizing inductances as seen by both windings at 50 Hz are given. Note: to ensure the accuracy of the equivalent circuit, it is important to include the mutual, inductive and capacitive, coupling effects between the two windings [18]. The frequency resolution for all the FRA plots in this paper is provided in TABLE 2.

The magnetizing inductance is frequency dependent, and to reflect this attribute, the measurement results for the complex relative permeability of silicon steel lamination were extracted from [19] and a nonlinear regression algorithm is used to determine the ''per unit value of measured relative permeability against frequency'' as presented in **FIGURE 2**.

TABLE 1. Electrical components of network model and their total values.

Electrical components			Total value
LV	Winding capacitance to ground	CgL (pF)	5640.1
	Winding series capacitance	CsL (pF)	5.67
	Winding air core inductance	L_{airLV} (mH)	1.58
	Winding magnetising inductance	L_{CORELV} (H)	0.72
HV	Winding ground capacitance	CgH (pF)	482.15
	Winding series capacitance	CsH (pF)	401.14
	Winding air core inductance	L_{airHV} (mH)	637.62
	Winding magnetizing inductance	L_{COREHV} (H)	90.03
Winding Interaction	Interwinding capacitance	C_{HL} (pF)	453.58
	Mutual magnetizing inductance	M_{core} (H)	8.05
	Mutual air core inductance	M_{air} (mH)	14.75

TABLE 2. Frequency resolution for all FRA plots in this paper.

Frequency range	Frequency resolution
10 Hz-2 kHz	5 Hz
2 kHz-20 kHz	50 Hz
20 kHz-200 kHz	0.5 kHz
200 kHz-1000 kHz	5 kHz

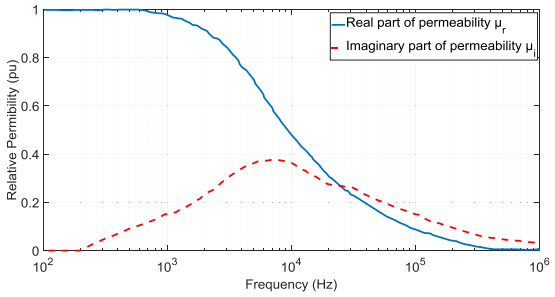

FIGURE 2. Per unit representation of measured relative permeability of electrical steel core material against frequency.

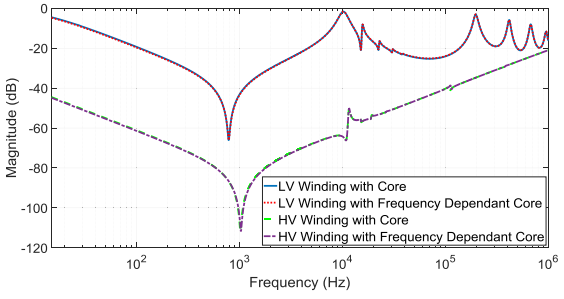

FIGURE 3. Comparison of FRA plots between constant and frequency dependent magnetizing inductances.

As a result, the frequency dependent magnetizing inductance is represented by $L_{core}(\mu_r + \mu_i)$.

Simulations were performed using both constant and frequency dependent magnetizing inductances. Their comparison is shown in **FIGURE 3**, which demonstrates considering frequency dependent magnetizing inductance or not has a negligible effect. This is because μ_r has a negligible difference for frequencies lower than 1 kHz and winding capacitances also have shown their effects by jointly creating the 1st anti-resonance at around 1 kHz. For higher frequencies, the magnetizing inductance behaves as large shunt impedance, losing its dominating status to the air core inductance and winding capacitances. Therefore the magnetizing inductance is regarded as a constant value in the following simulation scenarios.

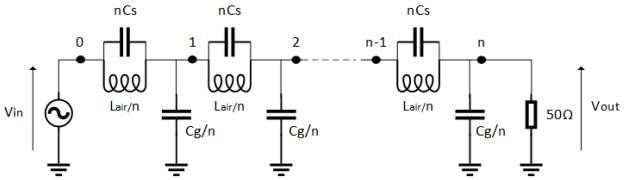

FIGURE 4. n-stage lumped-element LC ladder network of single winding.

In **FIGURE 3**, the frequency response of the HV winding has a lower magnitude than the LV winding, and the LV winding has multiple oscillations in the high frequency region whilst the HV winding has only a few resonant frequencies, which exactly accord with their winding characteristics.

III. SINGLE WINDING FRA INTERPRETATION

According to both the IEEE and IEC standards [15], [16], the FRA spectra can generally be divided into four frequency regions, the lowest is dominated by the transformer core, the next by the winding interactions, then the structure of the winding-under-test and finally the highest by the measurement set-up. The ''structure of the winding-under-test'' region is mainly analyzed to determine winding deformation.

Modeling approach has a greater flexibility of parameter manipulation, which allows separating the electromagnetic and electrostatic effects of the grounded core. Firstly the transformer is disassembled into two single air core windings, which are then used to quantify the influence of each electrical winding component. Secondly, the complexity is gradually increased by taking the iron core into account, and then mutual coupling between parts of the winding.

A. TYPICAL FREQUENCY RESPONSE OF SINGLE AIR CORE WINDING

Irrespective of the winding structure, any winding can be categorized into two types based on its α value, $\alpha = \sqrt{\frac{C_g}{C_s}}$. One has a high C_s hence small α type (e.g. interleaved disc winding), and the other has a low C_s hence large α type (e.g. plain disc or single helical winding). The value of α is mainly controlled by variation of C_s, as a winding with a fix voltage would have similar values of C_g which is dominated by the main insulation clearance between the winding and ground.

The simplest high frequency winding model consists of an n-stage lumped-element LC ladder network as shown in **FIGURE 4**, where the effect of mutual inductances between the units are taken into account by L_{air} as a lumped parameter rather than explicit representation, to ensure the use of analytical solutions to demonstrate the general patterns of frequency responses.

A general solution for voltage v and current i at any point $x, (x = 1, 2, \ldots n)$ of the network shown in **FIGURE 4** is developed in [6], [21]–[23] and reproduced in APPENDIX

TABLE 3. Comparison between frequencies from FRA simulation and derived equations (1) and (2).

Windings	k	f_k (kHz)		f_{0k} (kHz)	
		FRA	Equations	FRA	Equations
LV winding	1	166	166.6	83.5	83.6
	2	330	328.4	250	248.4
	3	480	481.3	405	406.2
HV winding	1	9.3	9.4	8.65	8.16
	f_c	FRA		Equation	
		9.95		9.95	

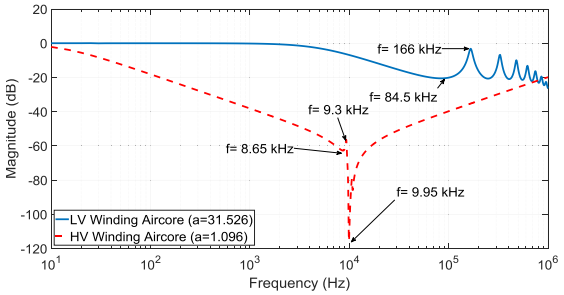

FIGURE 5. Typical FRA responses of single air core windings.

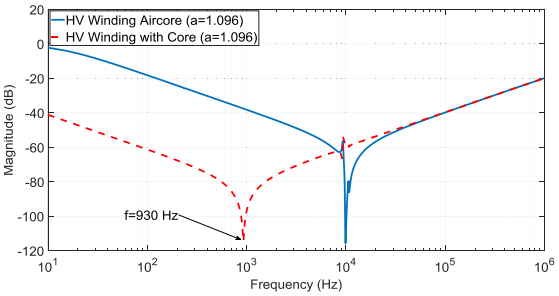

(a) FRA response of HV winding with core

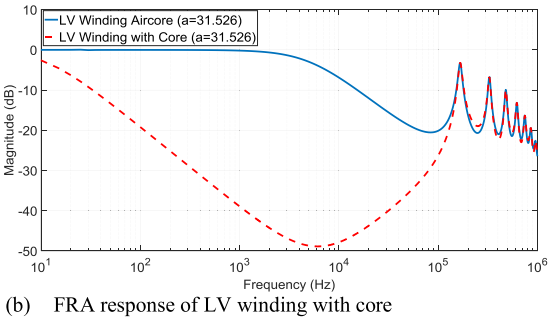

(b) FRA response of LV winding with core

FIGURE 6. Typical FRA responses of single windings with core.

for continuity and completeness. Here, the space coefficient α is explicitly expressed in the rewritten equations of resonant and pseudo anti-resonant frequencies, (1) and (2), to demonstrate its influence on the patterns of frequency responses:

$$f_k = \frac{1}{2\pi\sqrt{L_{air}C_s}}\frac{1}{\sqrt{1+\frac{\alpha^2}{(k\pi)^2}}} \tag{1}$$

$$f_{0k} = \frac{1}{2\pi\sqrt{L_{air}C_s}}\frac{1}{\sqrt{1+\frac{4\alpha^2}{((2k-1)\pi)^2}}}$$
$$k = 1, 2, \ldots (n-1) \tag{2}$$

FIGURE 5 shows LV and HV winding FRA plots, where each belongs to one catagory. For LV winding with a large α, approximately 31, its FRA features multiple resonances and 'U shape' pseudo anti-resonances between the adjacent resonances [6], [20]. The FRA of an HV winding with a small α, approximately 1, one critical anti-resonance occurs at 9.95 kHz and at higher frequencies, a smooth rising amplitude trend can be seen, with significantly fewer resonances.

TABLE 3 compares the frequencies of resonances and pseudo anti-resonances obtained from the FRA simulation and those calculated by (1) and (2).

When analyzing **FIGURE 5** and TABLE 3, it can be observed α has a dominating effect on the shape of FRA curve; when α is small, there are no multiple resonances expected as the terms $\frac{\alpha^2}{(k\pi)^2}$ in (1) and $\frac{4\alpha^2}{((2k-1)\pi)^2}$ in (2) are too small to distinguish the resonant frequencies, f_{0k} and f_k from the critical frequency f_c. These equations mathematically explain why the winding with low series capacitance such as plain disc windings and single helical windings always have multiple resonances, whilst the winding with high series capacitance such as interleaved disc type winding always have fewer or no resonances.

B. TYPICAL FREQUENCY RESPONSE OF SINGLE WINDING WITH MAGNETIC CORE INCLUDED

The next step is to investigate the effect of the core by assuming a single winding is placed onto the transformer core. This is equivalent to all the units of **FIGURE 4** are now fully coupled with one and another through the main flux in iron core and the air core inductance represented by L_{air} remain the same as in section III-A. Hence the first anti-resonance in the low frequency region would appear for single windings with small α; this is the low frequency feature we normally see on transformer FRA responses, and a comparison is made between the frequency responses of the windings with and without the magnetizing inductance, as presented in **FIGURE 6**.

FIGURE 6 shows that due to the large value of magnetizing inductance, the magnitude of the HV winding frequency response at low frequencies has dropped by nearly 40 dB when compared to the air core situation. The first anti-resonance with the core is at 930 Hz. This 'V shape' first anti-resonance f_v is caused by the core and the bulk winding capacitances, can be approximated by (3), with a correction factor Δ that involves the space coefficient α of the winding, and the magnetic coupling factor β which depends on the main flux and air flux linkages between the different parts of the winding:

$$f_v = \frac{1}{2\pi\sqrt{L_T C_s}}\sqrt{\Delta}$$
$$a\Delta^4 + b\Delta^2 + c = 0$$
$$\Delta^2 = \frac{-b-\sqrt{b^2-4ac}}{2a}$$
$$a = \frac{(1-\beta)}{2}, b = \frac{\alpha^2\beta}{8} - 1, c = \frac{(1+\beta)}{2} \tag{3}$$

L_T is the sum of the magnetizing inductance and air core inductance of the winding, $L_T = L_{core} + L_{air}$, and the magnetic coupling factor is defined as $\beta = \frac{M_{12}}{L_{11}}$, where M_{12} is the mutual-element and L_{11} is the self-element of the inductance matrix of the winding model when n=2. In the case of the HV winding, β= 0.992, and the first anti-resonant frequency is approximated by (3) as f_v = 905 Hz, which is reasonably close to 930 Hz as shown in **FIGURE 6** (a). To clearly demonstrate the importance of involving the correction factor Δ, the base frequency of the parallel resonance controlled by C_s and of L_T is calculated as 835 Hz.

As for the LV winding, due to the smaller number of turns linked with the main flux in the core, its magnetizing inductance is too small to alter the domination of the large α, the FRA of the LV winding seen in **FIGURE 6** (b) has the so called 'U' shape curve. If this is compared with the frequency response of the single air core LV winding, it seems the first pseudo anti-resonant frequency has been shifted to a lower frequency due to the introduction of the magnetizing inductance, and there is no change in the other resonances. The so called 'U' shape at the core dominant low frequency region has been stated in [17], [20] as *"... in the intermediate frequency band (2-20 kHz), with the apparent absence of the usual first low frequency minima and maxima", and "... is not unique to shell form transformers, being occasionally seen for some core form units, e.g. delta connected HV windings"*.

Although the transformer core is introduced into the model, **FIGURE 6** clearly demonstrated the high frequency features on both the LV and HV winding FRA plots are only associated with the air core inductance, i.e. they do not change with the inclusion of the magnetizing inductance.

C. FREQUENCY RESPONSE OF SINGLE WINDING WITH MUTUAL COUPLING EXPLICITLY MODELED

Transformers are designed to ensure efficient operation by arranging for the primary and secondary windings to be magnetically strongly coupled; hence the mutual inductances between these windings and parts of the same winding are significant. Primary and secondary windings on the same limb share the same main flux, but experience different leakage fluxes. A fixed value of transformer impedance can be achieved by carefully designing the winding dimensions as well as the radial insulation distance between them. Consequently, magnetic coupling can only be accurately modeled by using the full $n \times n$ inductive matrix. Note the number of elements in this matrix can be varied according to the frequency region being investigated; as a rule of thumb, the higher the frequency and the more the oscillation, the larger the value of n would be required.

The next step is to represent mutual inductive coupling by accurately modeling the full inductance matrix of the air core winding. The air core mutual inductances between every two units in **FIGURE 4** is no longer lumped into L_{air}, instead they are calculated and distributed across the inductance matrix according to the winding geometry;

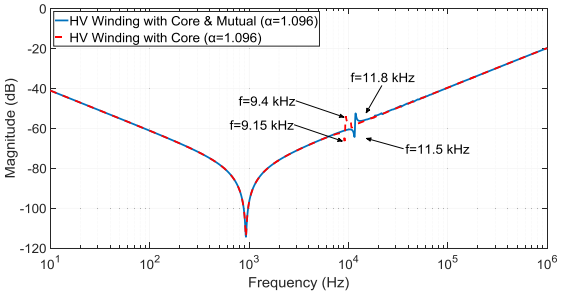

(a) FRA response of HV winding with mutual inductance explicitly modelled

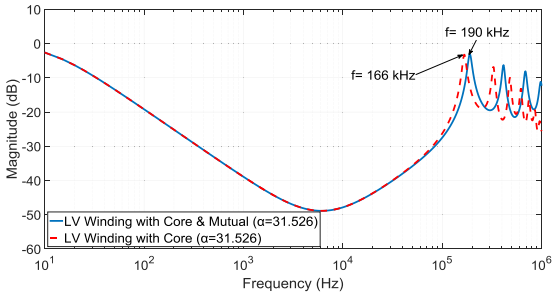

(b) FRA response of LV winding with mutual inductance explicitly modelled

FIGURE 7. Typical FRA responses of single windings with core and mutual inductance explicitly modeled.

meanwhile, the magnetizing inductance is also taken into account. **FIGURE 7** shows the effect of explicitly modeling the mutual inductances on the frequency responses of the LV and HV windings.

It can be seen that by taking mutual inductances explicitly into consideration, the resonant, anti-resonant and pseudo anti-resonant frequencies of the FRA in the high frequency region are all moved up to higher frequencies, as marked in **FIGURE 7** (a) and (b).

The section number n of the model determines the number of resonances in the corresponding FRA plot, i.e. n sections usually produce n-1 resonances as long as α is big enough; however having n + 2 elements in a model ensures the n^{th} resonance is obtained with reasonable accuracy. In this regard, the shift of the first resonance and anti-resonance in the high frequency region for both the LV and HV winding frequency responses can be quantified by applying a correction factor Δ_{air} into (1) and (2), the corrected equations are:

$$\begin{aligned} f_{1m} &= \frac{1}{2\pi\sqrt{L_{air}C_s}} \frac{1}{\sqrt{1+\frac{\alpha^2}{(k\pi)^2}}} \sqrt{\Delta_{air}} \\ f_{01m} &= \frac{1}{2\pi\sqrt{L_{air}C_s}} \frac{1}{\sqrt{1+\frac{4\alpha^2}{((2k-1)\pi)^2}}} \sqrt{\Delta_{air}} \\ \Delta_{air} &= 1+\beta_{air}, k=1 \end{aligned} \tag{4}$$

where f_{1m} and f_{01m} represent the first resonant and anti-resonant frequencies in the high frequency region after considering mutual inductances in a full inductive matrix, and

TABLE 4. Results of high frequency 1st resonances/anti-resonance based on FRA and derived equations (4).

Winding	Scenario	Frequency	$\frac{f_{1m}}{f_1}$ & $\frac{f_{01m}}{f_{01}}$	$\sqrt{\Delta_{air}} = \sqrt{1+\beta_{air}}$
LV	f_{1m}	190 kHz	1.145	1.145
	f_1	166 kHz		
HV	f_{1m}	11.8 kHz	1.255	1.253
	f_1	9.4 kHz		
	f_{01m}	11.5 kHz	1.257	
	f_{01}	9.15 kHz		

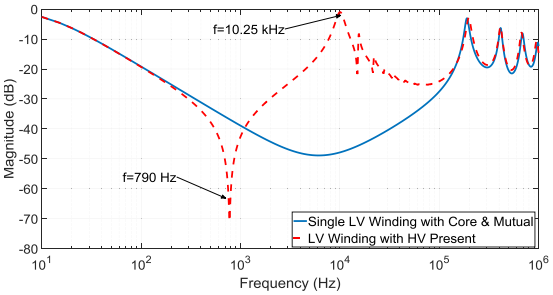

FIGURE 8. Comparison of LV winding FRA plots before and after HV winding is added.

$\beta_{air} = \frac{\sum_{i=1,j=1}^{i=n,j=n} M_{airij}}{\sum_{i=1}^{i=n} L_{airii}}$, L_{airii} is the air core self-inductance of unit i and M_{airij} is the air core mutual-inductance between unit i and unit j in the 3 stages winding model. The value for the LV winding is calculated as $\beta_{airLV} = 0.316$ and the value for the HV winding is calculated as $\beta_{airHV} = 0.565$; these are determined by the winding structure.

TABLE 4 gives the relationship of the first resonant and anti-resonant frequencies in the FRA plots with or without mutual inductance explicitly modeled. Equation (4) reconfirms the advantage of using a ratio of frequencies to reflect the frequency shifting [24]. Note the first anti-resonance in the low frequency region is mainly controlled by the core inductance and hence is not affected by mutual coupling. Therefore (3) is still valid for this scenario.

IV. INVESTIGATION OF FREQUENCY RESPONSES FOR SINGLE PHASE TWO-WINDING TRANSFORMER

Apart from the structure of the winding-under-test, the untested winding also influences the FRA spectrum through winding interaction. To demonstrate the influence of the untested winding on the FRA measurements of a transformer, the model described in **FIGURE 1** is used in this section.

The LV and HV winding FRA plots before and after they are placed onto a transformer core (with both windings included) is presented in **FIGURE 8** and **FIGURE 9**. The LV winding frequency response in the low and middle frequency regions is clearly affected by the HV winding; a typical 'V shape' anti-resonance f_v appears at 790 Hz, and a few new

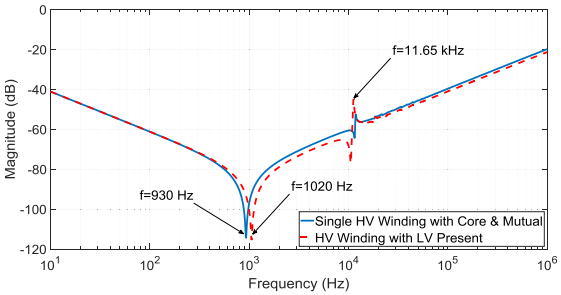

FIGURE 9. Comparison of HV winding FRA plots before and after LV winding is added.

resonances appear at 10.25 kHz and beyond, which is in the winding interaction dominant frequency region. However, the frequency shift observed in the HV winding frequency response when the LV winding is present, is minimal. The winding frequency responses in the high frequency region are dominated by the structure of winding-under-test and have negligible difference, which accords with the results presented in [15], [16].

The following sections focus on the impacts of the untested winding on the FRA measurement result, the impact can be divided into two parts according to the frequency region; first low frequencies dominated by the transformer core and then medium frequencies dominated by winding interaction.

A. LOW FREQUENCY REGION

The core dominated frequency region is conventionally regarded as frequencies less than 2 kHz, and generally a first anti-resonance exists for the FRA measurement results from the HV and LV windings. This indicates the conventional space coefficient α, seen for a single winding is no longer able to explain the low frequency characteristic of the FRA response for the windings in an actual transformer. As compared in **FIGURE 8**, the differences in the LV winding FRA plots before and after the winding is placed onto a transformer core is prominent. The plots show the FRA magnitude responses at frequencies lower than 100 Hz are not changed, but the newly created anti-resonance at 790 Hz is the definitive result of being coupled with the HV winding.

Simulation results indicate the winding FRA results in the low frequency region are not only determined by its magnetizing inductance and its own winding capacitances, but are also influenced by the un-tested winding capacitances resulting from winding interaction. This influence combined with the tested winding series capacitance produces the equivalent series capacitance C_{es} seen from the terminals of the tested winding. In addition, it is also natural to involve the concept of equivalent winding ground capacitance C_{eg} which defines the shunt capacitance to ground potential seen from the tested winding terminals. Hence the concept of α continues to be used for this single phase two-winding transformer, but is now redefined as $\alpha = \sqrt{\frac{C_{eg}}{C_{es}}}$, where C_{es} and C_{eg} can be approximately estimated using the four port equivalent circuit

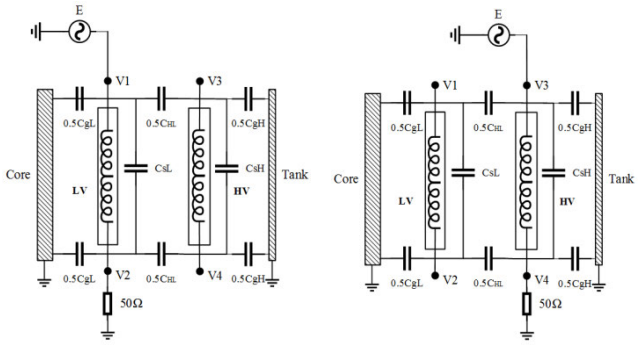

(a) LV end-to-end FRA measurement (b) HV end-to-end FRA measurement

FIGURE 10. Four port equivalent network of single phase two-winding transformer.

model of the single phase two-winding transformer, shown in **FIGURE 10**.

FIGURE 10 shows that because of the large voltage ratio between the HV and LV windings, which is similar to a generator transformer, the voltage difference induced in the untested winding is determined by the turns ratio and the potentials of the floating terminals can be estimated based on the equivalent capacitive network. Taking the circuit in **FIGURE 10** (a) as example, where V1 is fixed at 1 per unit by the measurement setup, the voltage difference V3-V4 is N per unit, where N is the turn ratio of HV to LV windings. However, the four port model of **FIGURE 10** is only valid for the analysis of the FRA plot in the low frequency region. Nevertheless, for a winding-under-test operating within a transformer, the resulting 'new' C_{es} and C_{eg} for both LV and HV windings can be estimated by (5) and (6), respectively, the detailed derivation of (5) and (6) can be found in [20].

Equation (5) helps explain why the equivalent winding series capacitance for a single helical winding is significant when it is used for the LV winding in a transformer with a large voltage ratio. (5) also provides insight on the 'equivalent' winding series capacitance as highlighted by the magnifying factor of ''turns ratio squared'' on the inter-winding capacitance as well as the series capacitance of the winding-not-under-test, and as a result, the equivalent space coefficient α is tremendously decreased. Using this insight it is observed the LV single helical winding in this transformer has a typical first anti-resonance as shown in **FIGURE 8**.

$$\begin{aligned} C_{es} &= C_{sL} + C_{sH}N^2 + \frac{(N^2 - 4N + 4)}{8}C_{HL} \\ C_{eg} &= C_{gL} + C_{gH} \text{ for LV winding} \end{aligned} \tag{5}$$

$$\begin{aligned} C_{es} &= C_{sH} \\ C_{eg} &= \frac{C_{HL} \times C_{gL}}{C_{HL} + C_{gL}} + C_{gH} \text{ for HV winding} \end{aligned} \tag{6}$$

However, when the HV winding is FRA tested as shown in **FIGURE 10** (b), the voltage difference V3-V4 is nearly 1 per unit at the first anti-resonance of the HV FRA spectrum. This is because 50 Ω is much smaller than the HV winding impedance, and the voltage difference V1-V2 is $\frac{1}{N}$ per unit according to the voltage ratio between windings.

TABLE 5. Equivalent C_{es}, C_{eg} and a of winding-under-test.

Equivalent parameters	LV winding	HV winding
Equivalent ground capacitance C_{eg} (pF)	6122.25	901.9
Equivalent series capacitance C_{es} (pF)	53896	401.14
Redefined $\alpha = \sqrt{\frac{C_{eg}}{C_{es}}}$	**0.337**	**1.499**

This means the influence of the LV winding series capacitance is negligible, thus the HV winding equivalent series capacitance remains the same before and after it is located near the LV winding, and the equivalent shunt capacitance to ground increases which ultimately increase its equivalent space coefficient α. Equation (6) helps our understanding of the reason for the small change in the first anti-resonance as shown in **FIGURE 9**.

The equivalent series and ground capacitances calculated by (5) and (6) are provided in TABLE 5 for both windings, and are then used to calculate the redefined equivalent space coefficient α.

The redefined space coefficient α in TABLE 5 confirms the earlier conclusion ''the space coefficient α determines the shape of the frequency response''. For this example, $\alpha = 0.337$ for the LV winding when the HV winding is involved and $\alpha = 1.499$ for the HV winding when the LV winding is involved. Such small values of α produce very clear 'V shape' anti-resonance in the low frequency region. In addition, the small change of α seen from the HV winding before and after involving the LV winding explains the relative small changes on the corresponding first anti-resonance. The calculated equivalent capacitances seen from the tested winding terminals and involving the redefined space coefficient α, allows (3) to be used to approximate the first anti-resonant frequencies of the LV and HV winding FRA plots in this single phase two-winding transformer. The calculated frequency of the first anti-resonance for the LV winding is 813 Hz, as compared with 790 Hz in **FIGURE 8**, and the calculated frequency of the first anti-resonance for the HV winding is 984 Hz, as compared with 1020 Hz in **FIGURE 9**, respectively. To clearly demonstrate the importance of involving the correction factor Δ in (3), the base frequencies of the parallel resonance controlled by C_{es} and of L_T are calculated, given as 808 Hz for LV winding and 837 Hz for HV winding. These approximations are reasonably close to the frequencies, indicating the validity of the equations and highlighting the relationships between the FRA characteristics and the electrical components in the equivalent circuit network.

B. INTERACTION IN MEDIUM FREQUENCY REGION

FIGURE 8 shows that the characteristics of the HV winding structure in the frequency region around 10 kHz, have been transferred through winding interaction, i.e. mutual inductive and capacitive couplings, to the LV winding FRA plot. However, **FIGURE 9** shows the LV winding has fewer turns, resulting in lower air core inductances and winding

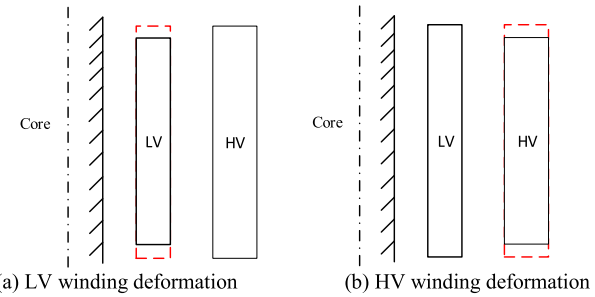

(a) LV winding deformation (b) HV winding deformation

FIGURE 11. Half axis-symmetric cross-sectional diagram of winding axial deformation.

capacitances, therefore it has minimal effect on the HV winding FRA plot. It can also be observed the first pseudo anti-resonance just after the frequency of 100 kHz, can be seen as a slight "kink" in the smooth capacitive rising magnitude slope of the HV FRA plot.

The medium frequency region is dominated by the interaction between the two windings, which is of interest when considering winding deformation occurring in the HV winding. It is reflected not only in the frequency response of the winding-under-test, but also in the frequency response of the untested winding in the medium frequency winding interaction region.

In this section, partial winding displacement in the axial direction is modeled individually for both windings. In the mid-part of the LV winding, the inter-turn distances from LV turn 27 to turn 48, counting from top to bottom, are decreased to 10% of the original value. In the mid-part of the HV winding, the inter-disc distances from HV disc 49 to disc 92, are decreased to 10% of the original value. Therefore the total height of LV winding decreases from the original 2.27 m to 2.13 m, and the HV winding shrinks from the original height of 2.28 m to 2.11 m, the shrinkage of winding is illustrated in **FIGURE 11**. **FIGURE 12** shows the frequency responses with and without the axial winding deformation.

In **FIGURE 12** (a), when the LV winding is partially axial-deformed, there is an observable left-shift of the resonance in the high frequency region for the LV winding frequency response. This region is dominated by the structure of the winding-under-test, whilst the frequency response of the HV winding shows almost no effect. This is understandable as the LV winding is 'weak' relative to the HV winding from the electrostatic and electromagnetic perspective, i.e. less turns means less inductance; and because of the simpler winding structure, smaller winding series capacitance.

However, when the HV winding is partially axial-deformed, both the HV and LV winding frequency responses show changes as given in in **FIGURE 12** (b). The HV FRA plot is affected in the low, medium and high frequency ranges by the deformation as the first anti-resonance shifts to the left from 1020 Hz to 960 Hz, and a pair of new resonance and anti-resonance are created at around 13.2 kHz, but for the LV winding, only the frequency responses in the low and medium frequency regions are impacted, the first anti-resonance shifts

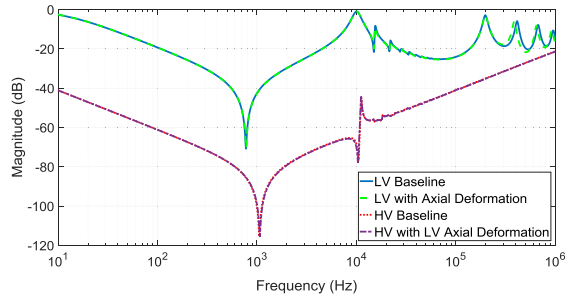

(a) Frequency responses with LV winding axial deformation

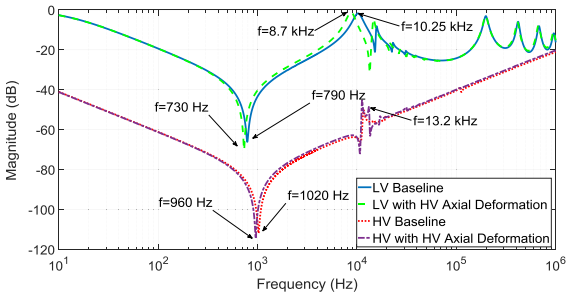

(b) Frequency responses with HV winding axial deformation

FIGURE 12. Frequency responses before and after winding axial deformation.

to the left from 790 Hz to 730 Hz, and the first resonance shifts from 10.25 kHz to 8.7 kHz. This is understandable as the deformation of HV winding, through inductive and capacitive coupling, passes its effect onto the frequency response of LV winding; however the high frequency "winding structure dominant" frequency region shows no difference in **FIGURE 12** (b), which is significant in interpreting the FRA measurement results.

The above results indicate that the medium frequency region of the 'unsuspected' winding frequency response can be used as a supplement to verify if deformation occurs on the other 'suspected' winding, especially when it is the 'strong' winding, here 'strong' means a winding has more turns hence larger inductance; and with a sophisticated winding structure which leads to bigger winding series capacitance.

Although only one example of axial deformation is simulated and analyzed here, it is recognized that many types of winding deformations such as tilting, spiraling and telescoping and radial deformation can be modeled to investigate the uniqueness of frequency response features associated with each type of deformation. For all cases, it is envisaged that the deformation of the 'strong' winding would pass its influence onto the frequency responses of the healthy windings in the winding interaction frequency region.

V. CONCLUSION

Mathematical equations are derived in this paper to reveal the relationships between the winding geometry dependent electrical components of the equivalent circuit network models and the resonant frequencies observed in FRA spectra. Air-core single windings were first modeled, and then more realistic scenarios developed in steps, by first adding the

core, then mutual inductive coupling in the same winding, and finally modeling a single phase two-winding transformer with mutual inductive and capacitive couplings between the windings. All the simulation results are provided to validate the developed equations.

Equations (1) and (2), developed in [6], [21]–[23] for a single air-core winding, are rewritten to explicitly express the space coefficient α and demonstrate its influence on the patterns of frequency responses. Equation (3) is derived to consider the magnetizing effect of an iron core on a single winding, and is then used to explain the first minimum as seen in the low frequency region of the measured FRA results. This minimum is dominated by the key parameters of magnetizing inductance and winding series capacitance, although the effects of mutual inductive coupling and the space coefficient of the winding should not be neglected. The significance of these effects is mathematically given by (3) and various case studies associated with this equation can be found in [25]. Mutual inductive coupling among units of a winding is important as it shifts the resonant and anti-resonant frequencies; (4) was derived to demonstrate the correction factor that needs to be applied to (1) and (2). This factor is determined by the magnetic coupling between parts of the air core winding.

In addition to analyzing single winding FRA characteristics, the frequency responses of the windings of a large voltage ratio single phase transformer, are also investigated. Equations (5) and (6) are developed to provide an insight on how to calculate the total values of the equivalent capacitances seen from winding terminals in a FRA standard test. This allows (3) to be used to approximate the first anti-resonant frequencies of the LV and HV winding FRA plots, proving the validity of the equations and highlighting the relationships between the FRA characteristics and the electrical components in the equivalent circuit network.

The equations developed in this paper provide an insightful quantitative relationship between the values of the electrical winding components and the corresponding FRA characteristics. They consequently help our understanding of FRA spectra and their interpretation.

VI. APPENDIX

In [6], [21]–[23], a general solution for voltage v and current i at any point x, $(x = 1, 2, \ldots n)$ of the lumped-element LC ladder network as shown in **FIGURE 4** is given as:

$$\begin{aligned} v(x, j\omega) &= A\cosh(rx) + B\sinh(rx) \\ i(x, j\omega) &= \frac{1}{Z}\left[A\sinh(rx) + B\cosh(rx)\right] \\ r^2 &= \frac{\frac{L_{air}C_g}{n^2}\omega^2}{1 - L_{air}C_s\omega^2} \\ Z &= \sqrt{\frac{L_{air}}{C_g(1 - L_{air}C_s\omega^2)}} \end{aligned} \tag{A.1}$$

where A and B are constants determined by the winding terminal conditions and x is the unit number along the winding starting from the injection side. A reasonable assumption is the winding impedance is significantly larger than 50 Ω, therefore at the winding terminals, $x = 0$ and $x = n$, the voltage potentials to ground are assumed as:

$$\begin{aligned} v(0, j\omega) &= A \\ v(n, j\omega) &= A\cosh(rn) + B\sinh(rn) = 0 \end{aligned} \tag{A.2}$$

With A and B obtained from (A2), the voltage ratio of the source and reference (V_{in}) to the response (V_{out}) can be calculated as:

$$\begin{aligned} \frac{V_{out}}{V_{in}} &= \frac{v(n, j\omega)}{v(0, j\omega)} = \frac{50}{Z}\frac{\sinh^2(rn) - \cosh^2(rn)}{\sinh(rn)} \\ &= \frac{-50}{Z\sinh(rn)} \end{aligned} \tag{A.3}$$

Note the denominators of both Z and r^2 contain $1 - L_{air}C_s\omega^2$, consequently (A3) has three different formats for different frequencies, as given:

$$\frac{V_{out}}{V_{in}} = \begin{cases} \dfrac{j50}{Z\sin(|r|n)}, f < \dfrac{1}{2\pi\sqrt{L_{air}C_s}} \\ \dfrac{1}{\infty}, f_c = \dfrac{1}{2\pi\sqrt{L_{air}C_s}} \\ \dfrac{50}{j|Z|\sinh(rn)}, f > \dfrac{1}{2\pi\sqrt{L_{air}C_s}} \end{cases} \tag{A.4}$$

$f_c = \frac{1}{2\pi\sqrt{L_{air}C_s}}$, is defined as the critical frequency. When $f < f_c$, Z is a monotonic function, thus $\sin(|r|n)$ oscillates between [-1,1] which forces the FRA magnitude to oscillate between capacitive and inductive, consequently multiple resonances are produced. When $\sin(|r|n) = 0$, the FRA magnitude reaches local maxima and resonances can be observed at the frequencies, f_k:

$$f_k = \frac{k\pi}{2\pi\sqrt{L_{air}C_g + (k\pi)^2 L_{air}C_s}}, k = 1, 2, \ldots (n-1) \tag{A.5}$$

When $\sin(|r|n) = \pm 1$, pseudo anti-resonances appear between two adjacent resonances, and the FRA magnitude reaches local minima. To complete the mathematical derivation above, a further development is implemented for pseudo anti-resonances at the frequencies of f_{0k}:

$$\begin{aligned} f_{0k} &= \frac{\left(\frac{2k-1}{2}\right)\pi}{2\pi\sqrt{L_{air}C_g + \left(\left(\frac{2k-1}{2}\right)\pi\right)^2 L_{air}C_s}} \\ k &= 1, 2, \ldots (n-1) \end{aligned} \tag{A.6}$$

When $f = f_c$, the FRA magnitude reaches the minimum, hence f_c is also called an anti-resonant frequency.

When $f > f_c$, $|Z|\sinh(rn)$ becoming monotonic and no oscillations are observed in the amplitude

response, this corresponds to the rising trend seen with a capacitor, i.e.:

$$\begin{aligned} Magnitude\,(dB) &= 20log_{10}\left(\left|\frac{V_{out}}{V_{in}}\right|\right) \\ &= 20log_{10}(100\pi f C_T) \\ C_T &= \frac{2\sqrt{C_g C_s}}{e^{\alpha}-e^{-\alpha}}, \alpha = \sqrt{\frac{C_g}{C_s}} \end{aligned} \tag{A.7}$$

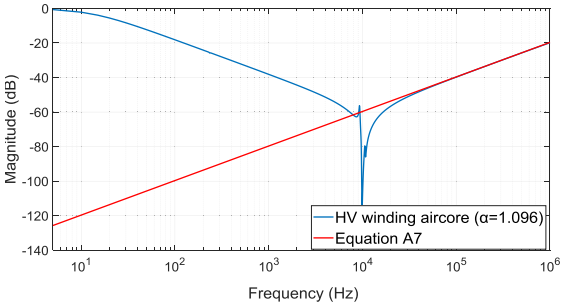

FIGURE A1. Frequency response of HV single aircore winding model and (A7) in representing the rising trend in high frequencies.

FIGURE A1 compares the frequency response produced by the HV single aircore winding model and (A7), and it shows the accuracy of (A7) in depicting the rising trend in high frequencies.

REFERENCES

[1] M. H. Samimi, S. Tenbohlen, A. A. Shayegani Akmal, and H. Mohseni, "Evaluation of numerical indices for the assessment of transformer frequency response," *IET Gener., Transmiss. Distrib.*, vol. 11, no. 1, pp. 218–227, Jan. 2017.

[2] S. Banaszak and W. Szoka, "Transformer frequency response analysis with the grouped indices method in End-to-End and capacitive inter-winding measurement configurations," *IEEE Trans. Power Del.*, vol. 35, no. 2, pp. 571–579, Apr. 2020.

[3] R. Rajamani, M. Rajappa, and B. Madanmohan, "Sweep frequency response analysis based diagnosis of shorts within transformer windings," *IET Gener., Transmiss. Distrib.*, vol. 11, no. 17, pp. 4274–4281, Nov. 2017.

[4] J. A. S. B. Jayasinghe, Z. D. Wang, P. N. Jarman, and A. W. Darwin, "Investigations on sensitivity of FRA technique in diagnosis of transformer winding deformations," in *Proc. Conf. Rec. IEEE Int. Symp. Electr. Insul.*, Sep. 2004, pp. 496–499.

[5] J. A. S. B. Jayasinghe, Z. D. Wang, P. N. Jarman, and A. W. Darwin, "Winding movement in power transformers: A comparison of FRA measurement connection methods," *IEEE Trans. Dielectr. Electr. Insul.*, vol. 13, no. 6, pp. 1342–1349, Dec. 2006.

[6] Z. D. Wang, J. Li, and D. M. Sofian, "Interpretation of transformer FRA responses—Part I: Influence of winding structure," *IEEE Trans. Power Del.*, vol. 24, no. 2, pp. 703–710, Apr. 2009.

[7] D. M. Sofian, Z. D. Wang, and J. Li, "Interpretation of transformer FRA responses—Part II: Influence of transformer structure," *IEEE Trans. Power Del.*, vol. 25, no. 4, pp. 2582–2589, Oct. 2010.

[8] A. Swee Peng, L. Jie, Z. D. Wang, and P. N. Jarman, "FRA low frequency characteristic study using duality transformer core modeling," in *Proc. Int. Conf. Condition Monitor. Diagnosis*, 2008, pp. 889–893.

[9] V. Nurmanova, M. Bagheri, A. Zollanvari, K. Aliakhmet, Y. Akhmetov, and G. B. Gharehpetian, "A new transformer FRA measurement technique to reach smart interpretation for inter-disk faults," *IEEE Trans. Power Del.*, vol. 34, no. 4, pp. 1508–1519, Aug. 2019.

[10] J. Liu, Z. Zhao, C. Tang, C. Yao, C. Li, and S. Islam, "Classifying transformer winding deformation fault types and degrees using FRA based on support vector machine," *IEEE Access*, vol. 7, pp. 112494–112504, 2019.

[11] B. Biswas and L. Satish, "Analytical expressions to link SCNF and OCNF of transformer windings to their inductances and capacitances for 1-Φ, 3-Φ Y and δ configurations," *IEEE Trans. Power Del.*, vol. 34, no. 4, pp. 1725–1735, Aug. 2019.

[12] M. M. Shabestary, A. J. Ghanizadeh, G. B. Gharehpetian, and M. Agha-Mirsalim, "Ladder network parameters determination considering nondominant resonances of the transformer winding," *IEEE Trans. Power Del.*, vol. 29, no. 1, pp. 108–117, Feb. 2014.

[13] F. Ren, S. Ji, Y. Liu, Y. Shi, and L. Zhu, "Application of Gauss–Newton iteration algorithm on winding radial deformation diagnosis," *IEEE Trans. Power Del.*, vol. 34, no. 4, pp. 1736–1746, Aug. 2019.

[14] R. Aghmasheh, V. Rashtchi, and E. Rahimpour, "Gray box modeling of power transformer windings based on design geometry and particle swarm optimization algorithm," *IEEE Trans. Power Del.*, vol. 33, no. 5, pp. 2384–2393, Oct. 2018.

[15] *Power Transformers—Part 18: Measurement of Frequency Response*, Standard IEC 60076-18, 2012.

[16] *IEEE Guide for the Application and Interpretation of Frequency Response Analysis for Oil-Immersed Transformers*, IEEE Standard C57.149-2012, 2013, pp. 1–72.

[17] *Mechanical Condition Assessment of Transformer Windings Using Frequency Response Analysis (FRA)*, Standard CIGRE Technical Brochure 342, 2008.

[18] P. A. Abetti and F. J. Maginniss, "Natural frequencies of coils and windings determined by equivalent circuit," *Trans. Amer. Inst. Electr. Eng. III, Power App. Syst.*, vol. 72, no. 3, pp. 495–504, 1953.

[19] K. G. N. B. Abeywickrama, T. Daszczynski, Y. V. Serdyuk, and S. M. Gubanski, "Determination of complex permeability of silicon steel for use in high-frequency modeling of power transformers," *IEEE Trans. Magn.*, vol. 44, no. 4, pp. 438–444, Apr. 2008.

[20] Z. D. Wang, B. Z. Cheng, P. A. Crossley, D. M. Sofian, and J. Sanchez, "Fundamental understanding offrequency response analysis 'U shape' through transformer modelling," presented at the CIGRE Joint Colloq. SC A2/B2/D1, New Delhi, India, 2019. [Online]. Available: https://www.cigreindia.org/colloquium2019/web/index.html

[21] Z. D. Wang, P. A. Crossley, K. J. Cornick, and D. H. Zhu, "An algorithm for partial discharge location in distribution power transformers," in *Proc. IEEE Power Eng. Soc. Winter Meeting.*, vol. 3, Feb. 2000, pp. 2217–2222.

[22] S. N. Hettiwatte, Z. D. Wang, and P. A. Crossley, "Investigation of propagation of partial discharges in power transformers and techniques for locating the discharge," *IEE Proc.-Sci., Meas. Technol.*, vol. 152, no. 1, pp. 25–30, Jan. 2005.

[23] Z. D. Wang, D. H. Zhu, P. A. Crossley, and K. J. Cornick, "Partial discharge location in power transformers," *IEE Proc.-Sci., Meas. Technol.*, vol. 147, no. 5, pp. 249–255, Sep. 2000.

[24] B. Z. Cheng, P. A. Crossley, Z. D. Wang, P. N. Jarman, A. Fieldsend-Roxborough, and G. Wilson, "Interpreting first antiresonance of FRA responses through low frequency transformer modelling," in *Proc. Int. Symp. High Voltage Eng.* Cham, Switzerland: Springer, 2020, pp. 982–992.

[25] B. Z. Cheng, X. Z. Mao, Y. X. Yang, Z. D. Wang, P. A. Crossley, and A. Fieldsend-Roxborough, "Factors dominating low frequency 'V, ∩, U' shape features in transformer FRA spectra," in *Proc. IEEE Int. Conf. High Voltage Eng. Appl.*, Beijing, China, Sep. 2020, Paper 10840.

BOZHI CHENG (Graduate Student Member, IEEE) received the B.Eng. degree in computer science from Central South University, China, in 2013, and the M.Sc. degree in electrical engineering from The University of Manchester, U.K., in 2017, where he is currently pursuing the Ph.D. degree with the Department of Electrical and Electronic Engineering. His main research interests include the study of transformer condition monitoring techniques, modeling and simulation, and frequency response analysis.

ZHONGDONG WANG (Senior Member, IEEE) received the B.Eng. degree in high voltage engineering and the M.Sc. degree in high voltage technologies from Tsinghua University, Beijing, China, in 1991 and 1993, respectively, and the Ph.D. degree in electrical engineering from UMIST, in 1999. She joined The University of Manchester (then UMIST), in 2000, where she is currently a Professor of High Voltage Engineering with the Electrical Energy and Power Systems Group, School of Electrical and Electronic Engineering. In July 2020, she is appointed as the new Pro-Vice Chancellor and Executive Dean of the College of Engineering, Mathematics and Physical Sciences, University of Exeter. Her current research interests include smart grids and low carbon electrical energy networks, in particular condition monitoring techniques, thermal, electrical transient and magnetic modeling techniques for power system networks, dielectric insulation ageing mechanisms, alternative environmentally friendly liquid insulating materials, and transformer asset management.

PETER CROSSLEY (Senior Member, IEEE) graduated from UMIST and the University of Cambridge. He joined GEC Measurements, in 1983, where he became a Senior Technical Engineer and later a Research Manager. Then, he moved to UMIST, in 1991, and subsequently progressed from Lecturer to Senior Lecturer to Reader. In 2002, he joined Queen's University, as a Professor of Electrical Engineering and as the Director of Power & Energy Research. Finally, he returned to The University of Manchester, in 2006, as a Professor of Power Systems. Later, he became the Director of the Joule Centre and the Head of Electrical Energy & Power Systems. He is currently the Director of the Centre for Doctoral Training (CDT) in Power Systems. As a Professor of Power Systems Engineering, he specializes in the protection and control of electrical power systems, impact of distributed/intermittent generators on electrical networks, and the design and use of renewable energy systems and smart-grids. In addition, he is a Convenor of CIGRE Working Group on Management of Protection Settings, a member of the Greater Manchester Energy Advisory Group, and the Chair of the IET Manchester Division and was the Vice-Chair of the IEEE ISGT Europe 2011 Conference. He is also a Distinguished Lecturer of the IEEE.